PHOTONICS Research

Design strategy of a high-performance multispectral stealth material based on the 3D meta-atom

Pingping Min,[1] Zicheng Song,[1] Tianyu Wang,[2] Victor G. Ralchenko,[1,3] Yurong He,[2] and Jiaqi Zhu[1,*]

[1]National Key Laboratory of Science and Technology on Advanced Composites in Special Environments, Harbin Institute of Technology, Harbin 150080, China
[2]School of Energy Science and Engineering, Harbin Institute of Technology, Harbin 150080, China
[3]Prokhorov General Physics Institute of Russian Academy of Sciences, Moscow 119991, Russia
*Corresponding author: zhujq@hit.edu.cn

Received 4 July 2023; revised 26 August 2023; accepted 1 September 2023; posted 5 September 2023 (Doc. ID 498640); published 1 November 2023

In this paper, a 3D meta-atom-based structure is constructed for the multifunctional compatible design of visible, infrared, and microwave. To achieve high performance, a novel dispersion tailoring strategy is proposed. Through the incorporation of multiple controllable losses within the 3D meta-atom, the dispersion characteristics are tailored to the desired target region. The effectiveness of the strategy is verified with an error rate of less than 5%. A proof-of-concept prototype is designed and fabricated, exhibiting high visible transparency, low infrared emission of 0.28, and microwave ultra-broadband absorption with a fractional bandwidth of 150% under 2.7 to 18.7 GHz. This work contributes a novel design strategy for the development of high-performance multispectral stealth materials with wide applications.

https://doi.org/10.1364/PRJ.498640

1. INTRODUCTION

Nowadays, with the rapid development of composite detection technology, multispectral function integration technology has become imperative in application scenarios such as aircraft cockpits [1–4]. In particular, there is a pressing need for high-performance multispectral stealth materials. High performance in terms of multispectral stealth materials refers to their excellent comprehensive performance, encompassing high transparency in the visible spectrum, low emission in the infrared spectrum, and broadband absorption in the microwave spectrum simultaneously [5–7]. However, conventional stealth materials such as composite nanofibers, conductive polymers, and doped oxide semiconductors are far from meeting the demands [8–11]. The key challenge lies in achieving multispectral functional compatibility, while further expanding microwave absorption bandwidth and enhancing angular stability [12–14].

Metamaterials, as artificial structures that are composed of periodically arranged subwavelength resonant units, can flexibly manipulate electromagnetic wave propagation [15–22]. By deliberately manipulating the constitutive parameters of metamaterials, electromagnetic response in different spectral regions can be controlled, opening a new path for multispectral stealth integration techniques [23–25]. Presently, the great majority of multispectral stealth materials are designed within the framework of 2D laminate structures composed of transparent materials. The most common approach is to achieve infrared stealth and microwave absorption by designing separate functional layers, respectively [26–29]. The underlying principle of the approach involves covering the microwave absorber with a high radar transmission metasurface that exhibits low infrared emissivity. However, the inclusion of a relatively large number of interface layers in separate designs significantly compromises visible transparency, typically resulting in only about 30% transmission, which hinders the achievement of a clear and unobstructed field of view in practical applications [26–28]. To improve visible transparency, some researchers have proposed sandwich structures with integrated functional layers for IR-radar stealth, but this comes at the cost of compromising IR and microwave stealth effects [30–33]. Obviously, these studies have not achieved high-performance multispectral stealth. It is evident that a well-designed structure is necessary to attain multispectral compatibility.

The pursuit of high performance, particularly in broadband microwave absorption, poses a significant challenge within the realm of multispectral compatibility. Currently, various methods are employed for expanding absorption bandwidth, including

equivalent circuit theory [34–36], interference theory [36–38], characteristic modes analysis [39–41], and optimization algorithms [42–44]. However, these methods have limitations. The equivalent circuit method encounters difficulties in modeling complex patterns or structures for analysis. Interference theory is confined to the analysis of multilayer structures. Characteristic modes analysis can be applied to broadband absorption designs involving lumped resistors but is unsuitable for impedance film-based absorption materials. Optimization algorithms, such as genetic algorithms and particle swarm algorithms, offer significant time and effort savings, yet they lack comprehensive insight and analysis of the physical nature. Therefore, a more versatile methodology is expected to guide microwave broadband absorption design, achieving genuine high-performance multispectral stealth.

In this work, we propose a new design strategy to develop high-performance multispectral stealth materials. The design strategy involves two key facets: constructing the 3D meta-atom structure for achieving multispectral functional compatibility and implementing the dispersion tailoring strategy to guide microwave broadband absorption design. Within the 3D meta-atom, we innovatively employ three-dimensional spatial functional partitioning to attain multispectral functional compatibility. This is achieved by employing horizontal components for infrared low emissivity and vertical components for microwave absorption. Meanwhile, the overall reduction of layers and interfaces facilitates visible high transparency. Furthermore, we propose a novel dispersion tailoring strategy based on Maxwell's equations to expand the microwave absorption bandwidth in grounded uniaxial structures. We validate the accuracy of the dispersion clipping strategy and its potential applicability to guide the design of other materials. Guided by the design strategy, we successfully design and fabricate a proof-of-concept prototype that demonstrates excellent comprehensive performance across the visible, infrared, and microwave spectra. The experimental measurement results strongly align with the simulation results, indicating its important role in various engineering applications, such as satellite solar panels, aircraft windows, and more.

2. DESIGN STRATEGY

This section is dedicated to elucidating the design strategy behind the multispectral stealth material of high performance. Initially, a 3D meta-atom with excellent potential for achieving multispectral compatibility is constructed, ensuring optimal functionality in visible and infrared bands. More importantly, a pioneering dispersion tailoring strategy is proposed, subsequently executed, and verified in the 3D meta-atom, thereby obtaining excellent microwave broadband absorption behavior, ultimately realizing a genuine high performance for multispectral stealth.

A. Multispectral Compatible Design: Construction of 3D Meta-Atom

To achieve optimal multispectral functional compatibility, we innovatively use the idea of 3D spatial functional partitioning, assigning horizontal and vertical components for distinct spectral realizations. This minimizes mutual interference and conflicts among different spectral realizations. Transparent materials are utilized throughout the structure to ensure overall optical transparency. When incident waves interact with the multispectral stealth material, the top layer plays a crucial role in shielding infrared light for effective infrared stealth and enabling microwave entry for subsequent absorption. To achieve this, we designed the planar infrared shielding layer (IRSL) that possesses low infrared emission and high microwave transmission as the topmost layer of the multispectral stealth material. Further, to achieve microwave absorption, the pillar structure formed by a standing-up impedance film cylindrical surface is employed, complemented by a backplane to eliminate microwave output. The pillar structure and backplane together constitute the microwave absorption unit (MAU). It is noteworthy that this vertical structure significantly reduces layers and interfaces, resulting in superior visible transparency compared to the 2D laminate structure, as demonstrated in previous studies [45]. Based on the above analysis, we construct the 3D meta-atom to achieve multispectral functional compatibility. The 3D meta-atom consists of the IRSL as the top layer and the MAU as the main body, as depicted in Fig. 1.

The proposed multispectral stealth material is formed by the basic unit cell 3D meta-atom arranged periodically in the horizontal direction, illustrated in Fig. 1. For a clearer presentation of structural particulars, consult the schematic of the 3D meta-atom in Fig. 2. Commonly, indium tin oxide (ITO) films are used as the functional layer to achieve multispectral compatibility, thanks to their high transparency in visible light, metal-like properties in the infrared band, and customizable sheet resistance [46–49]. The materials of the pillar and IRSL are ITO films with sheet resistance R_{s1} and R_{s2}, respectively. Within the MAU, the pillar is attached to the inner wall of the hole of polymethyl methacrylate (PMMA). The PMMA with periodic distribution of circular holes acts as the supporting layer, which has a relative permittivity of $2.25(1-j0.001)$. The Cu micromesh, characterized by exceptionally low sheet resistance of 1 Ω/sq and high optical transmittance of 86.5%, serves as the backplane to achieve zero microwave transmission and effectively improve the optical transparency. For further details, please consult our previous work [14,33]. Additionally, it should be noted that both the ITO film and the Cu micromesh were grown on the polyethylene terephthalate (PET) substrates with a relative permittivity of $3.0(1-j0.06)$. The PET substrate, with a thickness of less than 0.2 mm, has a negligible

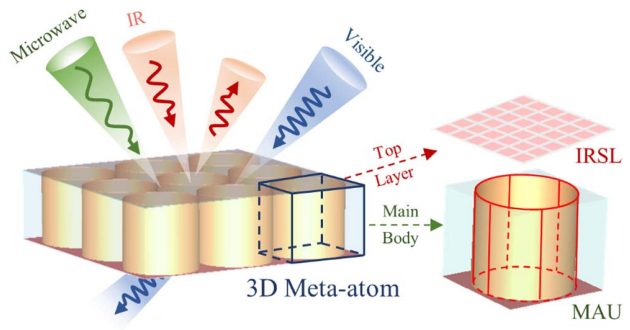

Fig. 1. Schematic of the 3D meta-atom-based multispectral stealth material.

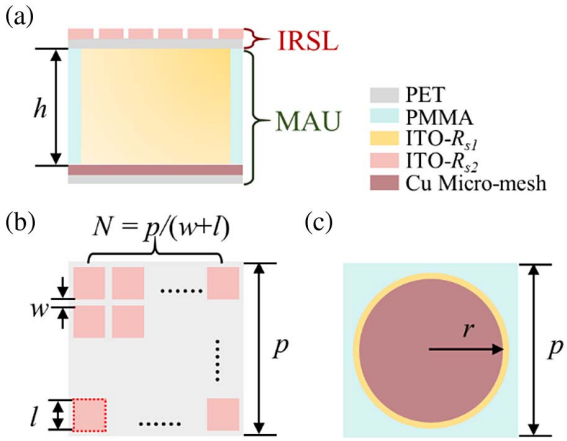

Fig. 2. Schematic of the 3D meta-atom: (a) side view of the 3D meta-atom, (b) top view of the IRSL, (c) top view of the MAU.

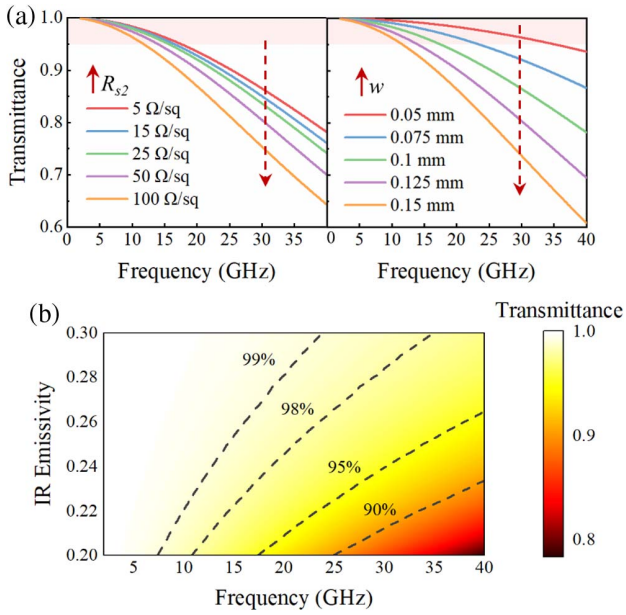

Fig. 3. Design of the IRSL. (a) The simulated transmittance of the IRSL with respect to frequency for various R_{s2} and w. (b) The correlation chart between the IR emissivity and microwave transmittance spectra for IRSL design.

impact on the performance of the multispectral stealth material due to its thinness.

The IRSL, as the first layer of incident wave encounters, is of critical importance in the multispectral stealth material. It is important to ensure both low IR emissivity to achieve IR stealth and high transmittance in the microwave band to allow more microwaves to enter in preparation for subsequent microwave absorption design. For this purpose, we etched the ITO film with a sheet resistance value of R_{s2} into a periodically arranged square patch array to serve as the IRSL. The schematic diagram of the IRSL unit is shown in Fig. 2(b). There are $N \times N$ square patches arranged periodically, the side length of the square patch is l, and the gap between adjacent patches is w. In the infrared band, the emissivity of the IRSL ($\varepsilon_{\mathrm{IRSL}}$) can be calculated as [50–52]

$$\varepsilon_{\mathrm{IRSL}} = \varepsilon_{\mathrm{ITO}} s_{\mathrm{ITO}} + \varepsilon_{\mathrm{PET}}(1 - s_{\mathrm{ITO}}), \tag{1}$$

where $\varepsilon_{\mathrm{ITO}}$ and $\varepsilon_{\mathrm{PET}}$ are the emissivity of ITO and its PET substrate, while s_{ITO} is the filling ratio of the ITO parts in the IRSL. Apparently, $\varepsilon_{\mathrm{IRSL}}$ is positively correlated with $\varepsilon_{\mathrm{ITO}}$ while negatively correlated with s_{ITO}. Previous studies have demonstrated a proportional relationship between $\varepsilon_{\mathrm{ITO}}$ and its sheet resistance [33]. In summary, a smaller R_{s2} and a larger s_{ITO} lead to a more effective IR stealth effect.

In the microwave band, the simulated curves of transmittance (T) for different R_{s2} (with constant $s_{\mathrm{ITO}} = 0.81$, $w = 0.1$ mm) and different gap w variation (with constant $s_{\mathrm{ITO}} = 0.81$, $R_{s2} = 5\ \Omega/\mathrm{sq}$) at 2–40 GHz are obtained, as shown in Fig. 3(a). It can be intuitively seen that low sheet resistance is also beneficial to get higher microwave transmittance, while under the condition of achieving the same $\varepsilon_{\mathrm{IRSL}}$, smaller gap w values lead to higher microwave transmittance. Therefore, considering the actual optional sheet resistance and etching processing accuracy, the optimal values for R_{s2} and w are determined to be $5\ \Omega/\mathrm{sq}$ and 0.05 mm, respectively. Further, to establish the correlation between calculated $\varepsilon_{\mathrm{IRSL}}$ and simulated T, a correlation chart is derived by controlling the last pending parameter l in the IRSL design, as shown in Fig. 3(b). The calculation procedure for $\varepsilon_{\mathrm{IRSL}}$ is elaborated in detail in the previous study [33]. The black dashed lines in the figure are the boundary lines for T values of 0.99, 0.98, 0.95, and 0.9, respectively. Using the correlation chart, it becomes easier to identify the optimal IRSL design that fulfills the requirements for both IR stealth and microwave absorption. In this work, the parameters of $R_{s2} = 5\ \Omega/\mathrm{sq}$, $l = 0.45$ mm, and $w = 0.05$ mm are adopted, which not only enables the attainment of a low IR emissivity of 0.25 but also ensures the microwave transmittance exceeding 98.3% across the entire 2–20 GHz.

B. Achieving High Performance: Strategy for Dispersion Tailoring

In general, the reflection and absorption characteristics of the grounded uniform uniaxial structure can be characterized by the structural constitutive parameters, that is, the equivalent relative permittivity tensors $\varepsilon_r = \mathrm{dig}(\varepsilon_{rx}, \varepsilon_{ry}, \varepsilon_{rz})$ and relative permeability tensors $\mu_r = \mathrm{dig}(\mu_{rx}, \mu_{ry}, \mu_{rz})$ [53,54]. Based on Maxwell's equations, the reflection coefficient of the grounded uniform uniaxial structure under normal incidence can be analytically solved in the form of an S parameter [55]:

$$S_{11} = \frac{-\sqrt{\varepsilon_{ry}\mu_{rx}}\cos(k_0\sqrt{\varepsilon_{ry}\mu_{rx}}h) - i\mu_{rx}\sin(k_0\sqrt{\varepsilon_{ry}\mu_{rx}}h)}{\sqrt{\varepsilon_{ry}\mu_{rx}}\cos(k_0\sqrt{\varepsilon_{ry}\mu_{rx}}h) - i\mu_{rx}\sin(k_0\sqrt{\varepsilon_{ry}\mu_{rx}}h)}, \tag{2}$$

where h is the thickness of the structure. Under the condition of $\varepsilon_r = \mu_r$ (i.e., $\varepsilon_{rx} = \varepsilon_{ry} = \mu_{rx} = \mu_{ry}$ and $\varepsilon_{rz} = \mu_{rz} = 1$), the perfect absorption occurred at the normal incidence angle for both the TE and TM polarizations.

Compared to perfect absorption, deriving the broadband absorption condition with an absorbance of over 90% holds greater interest and significance. In the case of the polarization-insensitive structure, $\varepsilon_{rx} = \varepsilon_{ry}$ and $\mu_{rx} = \mu_{ry}$. Typically, ε_{rz} and μ_{rz} are both taken as 1, whereas ε_{ry} is represented

as $\varepsilon_{ry} = \varepsilon'_{ry} + i\varepsilon''_{ry}$ and μ_{rx} is represented as $\mu_{rx} = \mu'_{rx} + i\mu''_{rx}$, where ε'_{ry} and ε''_{ry} are the real and imaginary parts of ε_{ry}, and μ'_{rx} and μ''_{rx} are the real and imaginary parts of μ_{rx}, respectively. It follows that the complex tensor of the constitutive parameters can be effectively determined essentially using four scalar values: ε'_{ry}, ε''_{ry}, μ'_{rx}, and μ''_{rx}. Furthermore, the constitutive parameter $\chi(\omega)$ of the structure, either the permittivity $\varepsilon(\omega)$ or the permeability $\mu(\omega)$, must obey the K-K relations [56–58]:

$$\mathrm{Re}(\chi(\omega)) = 1 + \frac{2}{\pi}\int_0^{+\infty} \mathrm{d}\omega' \mathrm{Im}(\chi(\omega'))\omega'/(\omega'^2 - \omega^2), \quad \textbf{(3)}$$

$$\mathrm{Im}(\chi(\omega)) = \frac{-2\omega}{\pi}\int_0^{+\infty} \mathrm{d}\omega' (\mathrm{Re}(\chi(\omega')) - 1)/(\omega'^2 - \omega^2). \quad \textbf{(4)}$$

According to the K-K relationship, the modulation of the real or imaginary part of a frequency-dependent constitutive parameter allows control over the other part, enabling a reduction of the four scalars for determining constitutive parameters to just two: ε''_{ry} and μ''_{rx}. Consequently, modulating these two imaginary parts accomplishes the desired manipulation of the constitutive parameters. Investigation into the impact of ε''_{ry} and μ''_{rx} variations on microwave absorption can yield valuable insights into the effects of these parameters, providing guidance for designing broadband absorption. It is noteworthy that positive values of ε''_{ry} and μ''_{rx} are essential for inducing wave attenuation.

Thus, the absorption behavior resulting from simultaneous variation in the imaginary parts of relative permittivity (ε''_{ry}) and relative permeability (μ''_{rx}) on the structure with $h = \lambda/10$, as described by Eqs. (2)–(4), is deduced and presented in Fig. 4. When the imaginary parts of the constitutive parameters fall within the region bounded by the two red lines, it indicates that the predicted absorptivity (Pred. A) for the corresponding frequency is greater than 0.9. The dashed line represents the conditions for perfect absorption, aligning with the earlier analysis. Figure 4(b) reveals that the red boundary line gradually becomes straighter as the values of the two imaginary parts increase, with only a slight deviation observed when the imaginary part is small, as shown in Fig. 4(a). Based on the aforementioned analysis, the dispersion tailoring strategy is proposed to achieve microwave broadband absorption, specifically by delicately tailoring the dispersion and dissipation so that the constitutive parameters satisfy the region within the red line of Fig. 4(b).

Further, the proposed 3D meta-atom-based multispectral stealth material, as a grounded uniform uniaxial structure, can be designed for high performance according to the guidance of the strategy. For the resonance of a structure, the Q factor can be expressed as $Q = \omega_0 \times (P_T/P_L) = f_0/\Delta f$, where ω_0 and f_0 represent the resonant frequencies, Δf is the absorption bandwidth, while P_T and P_L stand for the stored and dissipated energy, respectively. It is observed that a higher sheet resistance of the pillar (R_{s1}) leads to reduced dissipated energy (P_L), thereby lowering the Q factor and broadening the absorption bandwidth. Consequently, the pillar's impedance can serve as the controlled dissipation within the 3D meta-atom to tune the Q factor. In this way, the electrical and magnetic resonances can be finely adjusted, thus tailoring flat dispersion of the constitutive parameters across a broad frequency range, and ultimately achieving broadband microwave absorption. For the purpose, four models were created by modifying the pillar's impedance to introduce different levels of loss, as detailed in Table 1. All four models share the same IRSL parameters and possess the dimensions of $r = 8.1$ mm, $h = 15$ mm.

To clearly show the effect of the dispersion control, the commercial Maxwell equation solver CST MWS was used to execute full-wave simulations to retrieve the dispersion of complex constitutive parameters for different models, as depicted in Fig. 5. In the process of controlling the dispersion, the material of the pillar within the 3D meta-atom was initially set to perfect electric conductor (PEC) to obtain the initial frequency of multiple resonance. In Model-I of Fig. 5, six magnetic resonances and six electrical resonances were found spanning the frequency range from 2 to 20 GHz, indicating that the 3D meta-atom structure itself possesses vast potential for generating multiple resonances with ultra-broadband absorption capabilities. After increasing the R_{s1} to 10 Ω/sq, the bandwidths of all resonances in Model-II become broadened. When the R_{s1} is further increased to 100 Ω/sq, the multiple magnetic and electrical resonances in Model-III become indistinguishable due to enhanced dissipation, resulting in both the imaginary and real parts becoming flatter. Furthermore, in Model-IV, with R_{s1} increased to 200 Ω/sq, the constitutive parameters exhibit even flatter behavior, particularly at lower

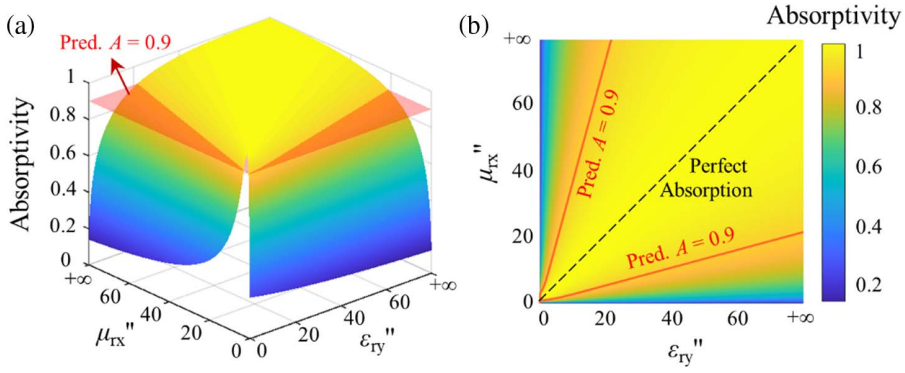

Fig. 4. Effect of variation in the imaginary part of relative permittivity and permeability on the absorptivity: (a) three-dimensional map; (b) two-dimensional map.

Table 1. Sheet Impedances of Different Models

Examples	Impedance	
	Pillar	IRSL
Model-I	PEC (no losses)	5 Ω/sq
Model-II	10 Ω/sq	5 Ω/sq
Model-III	100 Ω/sq	5 Ω/sq
Model-IV	200 Ω/sq	5 Ω/sq

frequencies. Concurrently, the real part of the normalized impedance approaches unity, while the imaginary part of the normalized impedance approaches zero throughout the frequency range, indicating the potential to achieve ultra-wide absorption [59].

Moreover, scatter distribution plots depicting the imaginary parts of the constitutive parameters within the 2–20 GHz range for the four models were obtained, as presented in Fig. 6. It is important to note that the yellow area corresponds to the region where the imaginary part of the constitutive parameters can be distributed to achieve predicted absorptivity values greater than 0.9, as observed in Fig. 4(b). Following the guidance of the dispersion tailoring strategy, scatters within the yellow region were labeled red, representing Pred. A at the corresponding microwave frequency greater than 0.9. Conversely, scatters outside the yellow region were labeled green, representing Pred. A less than 0.9, as shown in Fig. 6. It can be seen that as the R_{s1} increases, the proportion of red scatters in the distribution expands, indicating a wider predicted absorption bandwidth greater than 0.9 within the 2–20 GHz range, as supported by the quantitative data presented in Table 2. Apparently,

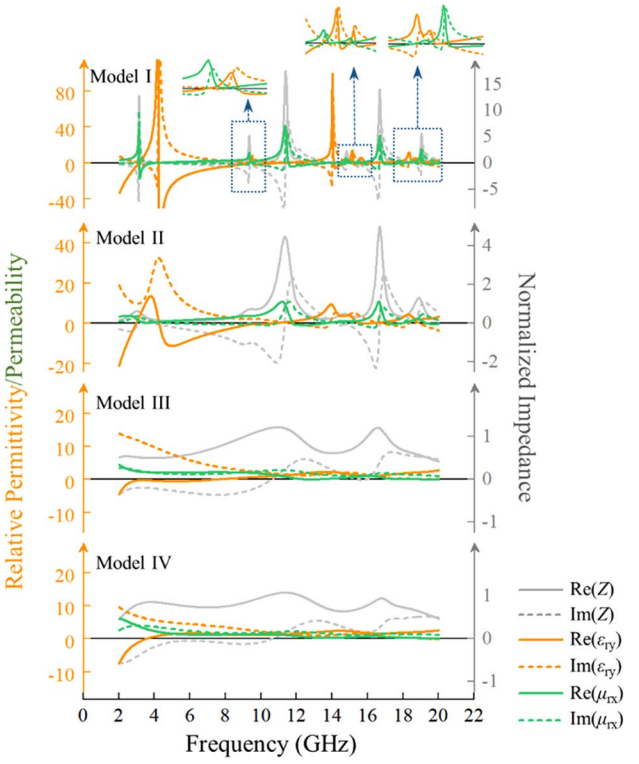

Fig. 5. Retrieved constitutive parameters and normalized impedance for different models.

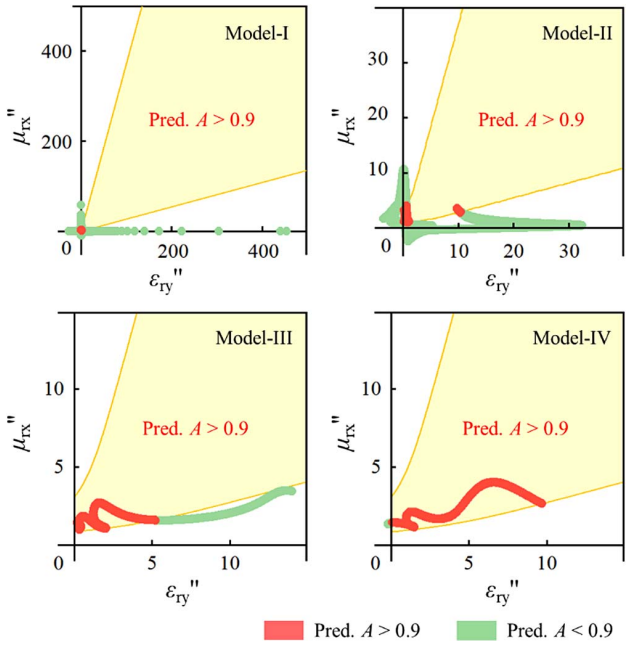

Fig. 6. Scatter distribution plots of the imaginary part of relative permittivity versus the imaginary part of relative permeability at frequencies from 2 to 20 GHz for different models (the yellow area indicates the range where predicted absorptivity is over 90%).

Model-IV exhibits the highest potential for achieving the broadest microwave absorption bandwidth, aligning with the analytical results obtained in Fig. 5.

To verify the accuracy of the dispersion tailoring strategy, simulated absorptivity (Sim A) for the four models across the 2–20 GHz range was obtained using the finite-element frequency-domain method in CST, as depicted in Fig. 7(a). It can be intuitively seen that the absorption becomes progressively better with increasing sheet impedance, where Model-IV has the best microwave broadband absorption. These conclusions are consistent with the results predicted by the proposed strategy. Moreover, Fig. 7(b) shows the simulation results of the power loss distribution ratio for the components in Model-IV. Notably, the majority of the power loss occurs on the pillar, while the power loss on the substrate gradually increases after 8 GHz, albeit remaining below 0.5%. The power loss for the remaining components is nearly negligible. This observation indicates that the introduction of controllable loss in the pillar, as envisioned in the proposed strategy, plays a crucial role in achieving broadband absorption performance. It validates the feasibility and rationale behind the design concept.

Furthermore, the accuracy of the proposed strategy is further verified by comparing and analyzing the prediction results with the simulation results for the four models. Through the comparison, it can be divided into four cases: both Pred. A and Sim A are greater than 0.9, both Pred. A and Sim A are less than 0.9, Pred. A is greater than 0.9 but Sim A is less than 0.9, and Pred. A is less than 0.9 but Sim A is greater than 0.9. To provide a more comprehensive view, the scatter distribution of the imaginary part of the constitutive parameters for different models across the 2–20 GHz range in Fig. 6 is further refined by incorporating the simulation results, as depicted in Fig. 8.

Table 2. Quantitative Statistics on the Consistency of Predicted and Simulated Absorptivity for Different Models

Models	Pred. $A < 0.9$ and Sim $A < 0.9$	Pred. $A < 0.9$ and Sim $A < 0.9$	Pred. $A > 0.9$ but Sim $A < 0.9$	Pred. $A < 0.9$ but Sim $A > 0.9$	Accuracy
Model-I	0	98.1%	0.9%	1%	98.1%
Model-II	5.1%	92.5%	2.4%	0	97.6%
Model-III	60.6%	35.1%	3.5%	0.8%	95.7%
Model-IV	88.2%	7.3%	4.5%	0	95.5%

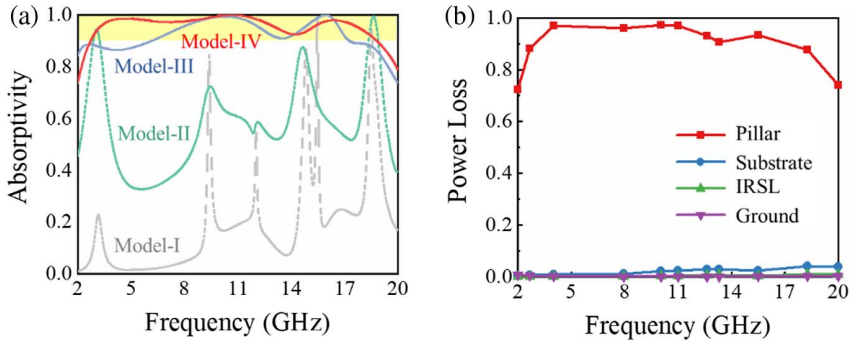

Fig. 7. (a) Simulated absorption curves for different models. (b) Simulated frequency-dependent power loss of the constituents in the 3D meta-atom for Model-IV.

For a clearer presentation, in Fig. 8 the scatter plot omits cases where both Pred. A and Sim A are less than 0.9 for clarity, while the pie chart only represents the percentage of the correctly predicted cases. The scatter plot in Fig. 8 visually demonstrates a strong agreement between the prediction and simulation results for all four models. Additionally, the pie chart in Fig. 8 clearly illustrates the distribution of the four cases within each model and reveals trends in the proportion of the same case among different models. For precise quantitative analysis, Table 2 presents the specific percentage distribution of these four cases for the different models. Statistically, the accuracy of predictions for all four models exceeds 95%, with an error rate of less than 5%, thereby confirming the accuracy and feasibility of the dispersion tailoring strategy in this study.

3. PROTOTYPE AND EXPERIMENTAL VERIFICATION

A. Proof-of-Concept Prototype

For demonstration, the best-performing Model-IV is taken for analysis and discussion. Considering the actual conditions of prototype fabrication, the final optimized parameters of the

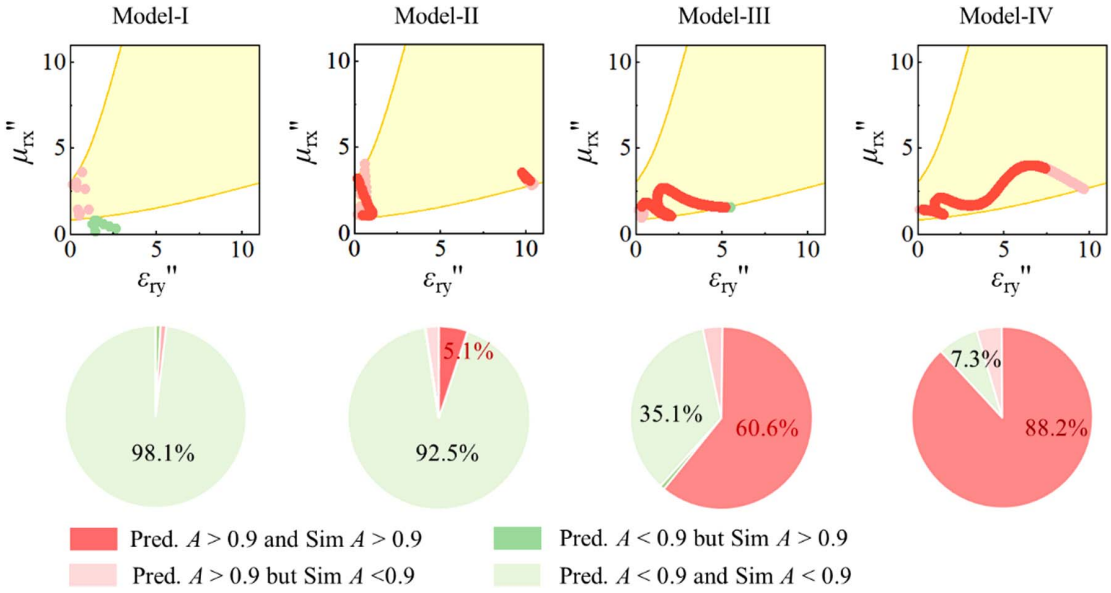

Fig. 8. Scatter distribution plots of the imaginary part of relative permittivity versus the imaginary part of relative permeability (top) and pie chart analysis on the consistency of predicted and simulated absorptivity (bottom) at frequencies from 2 to 20 GHz for different models.

proof-of-concept prototype are obtained as $R_{s1} = 200\ \Omega/\text{sq}$, $R_{s2} = 5\ \Omega/\text{sq}$, $p = 18$ mm, $l = 0.45$ mm, $w = 0.05$ mm, $r = 8.1$ mm, and $h = 15$ mm. In addition, the PET substrate thicknesses for the 5 Ω/sq ITO film, 200 Ω/sq ITO film, and Cu micromesh attachments are 0.175 mm, 0.05 mm, and 0.125 mm, respectively. Consequently, the comprehensive thickness of the 3D meta-atom is 15.3 mm, corresponding to $0.138\lambda_L$, where λ_L represents the lowest frequency of microwave absorption. In the infrared band, the prototype can achieve a low IR emissivity of 0.25, calculated using Eq. (1). Meanwhile, in the microwave band, the proof-of-concept prototype exhibits excellent absorption performance, demonstrating ultra-broadband absorption with an efficiency above 90% from 2.7 to 18.8 GHz (fractional bandwidth, FBW = 150%) at normal incidence, covering almost four continuous microwave bands of S, C, X, and Ku, as illustrated by the full-wave simulation results shown in Fig. 9(a).

Angular stability plays a crucial role in achieving effective broadband microwave absorption in practical applications. The curves in Fig. 9(b) depict the variation of the fractional bandwidth of TE and TM polarization with oblique incidence angles (theta) for TE and TM polarizations, offering a clear illustration of the prototype's angular stability. To gain more insight into the details, simulated absorption spectra under oblique incidence of TE and TM polarizations are demonstrated, as shown in Fig. 10. The absorption performance under TE polarization maintains a broadband absorption with an FBW exceeding 120% within a 50° range. In comparison, the absorption performance under TM polarization is even more remarkable. Within a 60° range, the FBW surpasses 150% and even exceeds vertical incidence between 28° and 58°, reaching a maximum FBW of 154%. Evidently, the prototype exhibits stronger absorption under TM polarization at larger incidence angles compared to TE polarization. This discrepancy arises from variations in the magnetic field component at the incident surface. Under TE polarization, the magnetic field component at the incident surface decreases as the incidence angle increases, resulting in a weakening of the

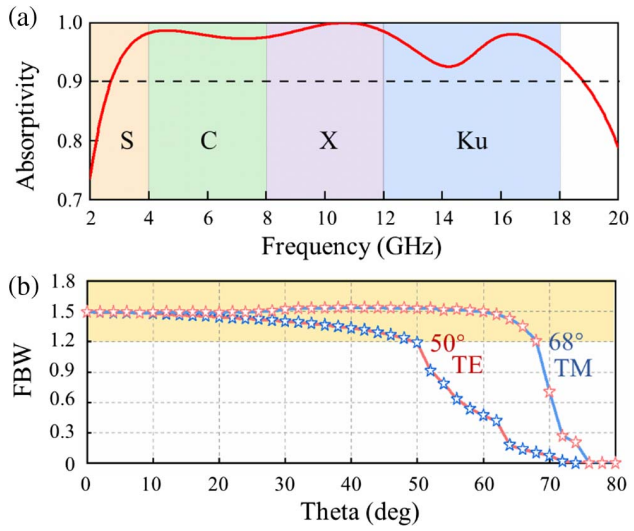

Fig. 9. (a) Simulated absorption curve and (b) simulated variation curves of FBW with oblique incidence angles under TE and TM polarizations for the proof-of-concept prototype.

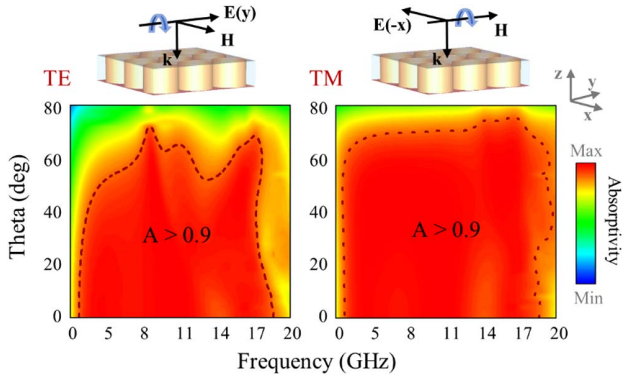

Fig. 10. Simulated absorptivity of the proof-of-concept prototype under oblique incidence with TE and TM polarizations.

magnetic resonance. Conversely, TM polarization maintains a stable magnetic field component at the incident surface, ensuring a more stable absorption capacity as the incidence angle increases. Overall, these results indicate that the proof-of-concept prototype demonstrates superior angular stability. Moreover, the prototype possesses the advantage of polarization independence, owing to its four-fold rotational symmetry.

Table 3 presents a performances comparison of the proposed prototype based on the 3D meta-atom with recently reported multispectral stealth materials from the literature. Here, in order to more intuitively compare and evaluate the comprehensive performance of multispectral stealth materials in different spectra of visible, infrared, and microwave, we define the figure of merit (FoM) as

$$\text{FoM} = \frac{\text{FBW}}{\varepsilon_{\text{meta}}} + T_{\text{optical}}, \tag{5}$$

where $\varepsilon_{\text{meta}}$ and T_{optical} correspond to "IR emissivity" and "optical transparency" in Table 3, respectively. The FoM clearly demonstrates the superiority of the proposed prototype, as its values significantly surpass those of previous research, justifying its classification as a "high-performance" solution. More importantly, the prototype exhibits substantial advantages in terms of broadband microwave absorption and angular stability, further validating the effectiveness and feasibility of the dispersion tailoring strategy.

B. Experimental Verification

To experimentally verify the performance of the proof-of-concept prototype, we fabricated a large-scale version dedicated to performance measurements, as illustrated in Fig. 11(a). This fabricated prototype has a surface area of 288 mm × 288 mm, encompassing 16 × 16 unit cells. The upper layer IRSL was fabricated by a laser carving of the commercial ITO film of 5 Ω/sq. For structural support, a custom-processed transparent PMMA, 15 mm thick, featuring periodically arranged circular holes, was used as an intermediate media layer. Then, ITO film of 200 Ω/sq was attached to the inner wall of the periodically arranged holes. The backplane consisted of the Cu micromesh with a low sheet resistance of 1 Ω/sq and an average optical transmittance of 86.5%, which was fabricated through selective electroplating of Cu into microgrooves imprinted on a PET

Table 3. Comparison with Other Multispectral Stealth Materials

Refs.	IR Emissivity	Bandwidth (GHz)	FBW	Angle Stability		Optical Transparency	Thickness	FoM
				TE	TM			
[27]	0.23	7.5–18	82.4%	~40°	~40°	~0.3	$0.112\lambda_L$	3.88
[28]	0.49	7.3–18.8	88.1%	Not mentioned		~0.25	$0.085\lambda_L$	2.05
[33]	0.53	8.9–16.4	59.3%	~30°	~30°	0.7	$0.068\lambda_L$	1.81
[60]	0.25	5.7–16.5	97%	~30°	~40°	Not mentioned	$0.073\lambda_L$	3.88
[61]	0.46	8–32	120%	~30°	~60°	0.54	$0.101\lambda_L$	3.14
[62]	0.3	8.7–32	115%	~30°	~45°	~0.6	$0.112\lambda_L$	4.43
This work	0.28	2.7–18.8	150%	50°	68°	0.66	$0.138\lambda_L$	6.02

substrate using roll-to-roll technology [43,63]. Finally, interlayer adhesion was achieved using an ultra-thin, insulating optically clear adhesive to maintain the overall structure's high optical transparency. As seen in Fig. 10(a), the fabricated prototype exhibits excellent transparency, allowing the naked eye to clearly view the images beneath it.

Further, Fig. 11 also displays the actual measurement results of the fabricated prototype in the IR, visible, and microwave spectra. Within the visible spectrum, the transmittance of the prototype can be assessable through a weighted calculation of the two cases shown in the inset of Fig. 11(b). The transmittance curves of visible light spanning 380–760 nm for the two cases were measured using the ultraviolet spectrophotometer, shown in Fig. 11(b). The red curve delineates the case wherein visible light traces the trajectory of the red dotted arrow, permeating the prototype's PMMA hole region. Similarly, the blue curve signifies an optical wave that aligns with the schematic of the blue dotted arrow, penetrating the portion of the prototype corresponding to the PMMA. The optical average transmittance for the red and blue curves from 380 to 760 nm is at 67.8% and 62.1%, respectively. In this work, the duty ratio of the PMMA, calculated as $\pi r^2/p^2 = 0.636$, yields an average optical transmittance of the prototype at 65.7%, which ensures high transparency performance for the naked eye.

Within the IR spectrum, the prototype's transmission and reflection spectra were measured using the Fourier transform infrared (FTIR) spectrometer, resulting in the obtained infrared emission curve displayed in the left half of Fig. 11(c). Within

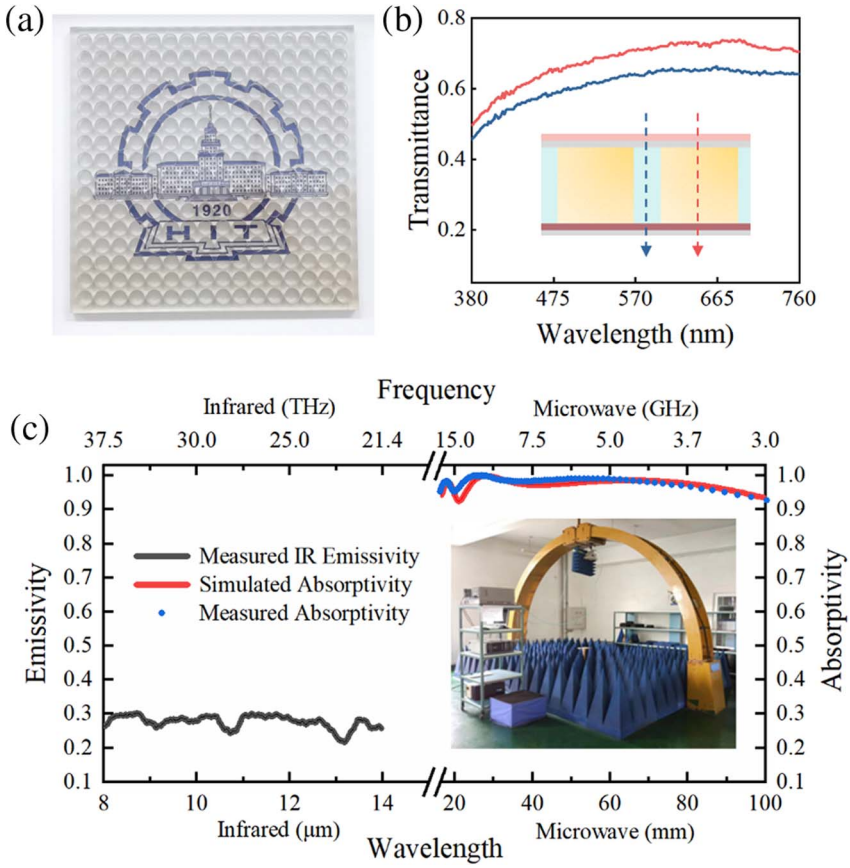

Fig. 11. Measurement results of the fabricated prototype. (a) Photographic image of the prototype. (b) Visible transmission measurement. (c) Measured IR emissivity spectra (left) and comparison of measured and simulated microwave absorptivity (right). Inset: photograph of microwave absorption performance measurement scenario.

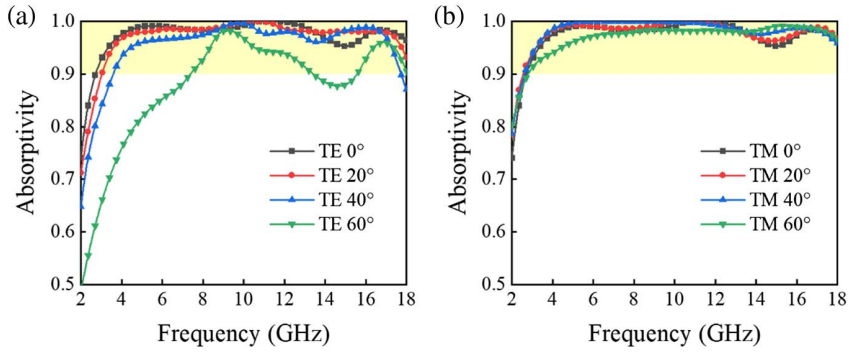

Fig. 12. Measured absorbance curves of the prototype under oblique incidence with (a) TE and (b) TM polarizations.

the 8–14 μm IR band, the average IR emissivity of the IRSL is measured to be 0.277, closely aligning with the predicted value of 0.25. Within the microwave spectrum, the reflectance coefficient ($|S_{11}|$) across the continuous 2–18 GHz frequency range was measured using the arch method, shown in the inset on the right side of Fig. 11(c). Due to zero microwave transmission from the Cu micromesh, the microwave absorptivity was deduced through $A = 1 - |S_{11}|^2$, thus yielding the microwave absorption curves. In the right half of Fig. 11(c), a comparison emerges between the measured and simulated microwave absorbance curves, spanning a wavelength range of 16.67 to 100 mm (18 to 3 GHz). The results demonstrate good agreement between the experimental and simulated data. Minor deviations between the simulated and measured microwave absorbance curves mainly arise from fabrication and assembly tolerances, measurement errors, and variations in the permittivity of the substrates. Additionally, Fig. 12 showcases the measured absorbance curves at oblique incidence angles of 0°, 20°, 40°, and 60° for both TE and TM polarizations, respectively. This presentation offers empirical evidence of the prototype's excellent wide-angle absorption characteristics.

To further assess the infrared stealth performance of the proof-of-concept prototype, we used an infrared thermal camera (TPH 16) to take infrared images in the range of 8–14 μm at elevated temperatures, as shown in Fig. 13. For detailed test procedures, refer to our previous work [33]. The surface temperature of the 60 mm × 60 mm glass placed atop the thermal plate is evenly distributed and maintained at 90°C, as illustrated in Fig. 13(a). As reference samples, three identically sized specimens (60 mm × 20 mm) were prepared: continuous ITO (5 Ω/sq), IRSL, and PET. These samples were arranged as shown in Fig. 13(b) and simultaneously placed on the heated glass substrate. After being stabilized, their temperatures were measured at 36.4°C, 48.2°C, and 84.5°C, respectively, as depicted in Fig. 13(b). The observed results indicate that the proposed IRSL exhibits an emissivity similar to that of the continuous ITO film.

The surface emissivity can be calculated by the equation [64]

$$\varepsilon = (T_r^4 - T_a^4)/(T_0^4 - T_a^4), \tag{6}$$

where T_r is the temperature measured by the IR thermal camera (48.2°C), T_a is the ambient temperature (25°C), and T_0 is

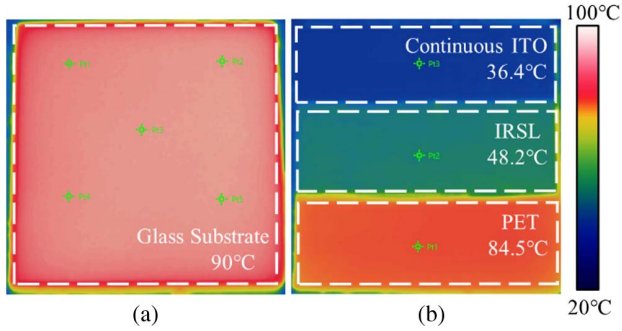

Fig. 13. Thermal infrared image of (a) glass substrate with uniform temperature distribution on the thermal plate and (b) continuous ITO, IRSL, and PET on the glass substrate.

the true temperature (90°C). According to Eq. (6), the IR emissivity of the IRSL is calculated to approach 0.29, which is close to the measured value of 0.277.

These results demonstrate the ability of the IRSL to maintain low levels of IR radiation, even under high-temperature conditions, making it suffer to detect using IR detection equipment.

4. CONCLUSION

In this work, a high-performance multispectral stealth material is developed based on the constructed 3D meta-atom, guided by an innovative dispersion tailoring strategy. By introducing multiple controllable losses into the multispectral compatible 3D meta-atom structure, the dispersion is precisely tailored to align the intrinsic parameters with the requirements of the dispersion tailoring strategy, resulting in excellent comprehensive performance. To demonstrate, a proof-of-concept prototype was fabricated, exhibiting a high visible transmittance of 0.66, low infrared emission of 0.28, as well as ultrabroadband microwave absorption (FBW = 150%) from 2.7 to 18.7 GHz covering the continuous microwave bands of S, C, X, and Ku. Additionally, it also has remarkable angular stability, maintaining FBW over 120% of microwave ultrabroadband absorption within 50° and 68° for TE and TM polarizations, respectively. The outstanding comprehensive performance of the proposed multispectral stealth material will

make it extremely useful for many engineering applications. Moreover, the dispersion tailoring strategy proposed can be extended to guide microwave broadband absorption in other homogeneous uniaxial materials.

Funding. Open Fund of Key Laboratory (JZX7Y201911SY008601); Key Project of National Natural Science Foundation of China (52032004); National Natural Science Foundation for Distinguished Young Scholars of China (51625201).

Disclosures. The authors declare no conflicts of interest.

Data Availability. Data underlying the results presented in this paper are not publicly available at this time but may be obtained from the authors upon reasonable request.

REFERENCES

1. G. A. Rao and S. P. Mahulikar, "Integrated review of stealth technology and its role in airpower," Aeronaut. J. **106**, 629–641 (2002).
2. E. F. Knott, J. F. Shaeffer, and M. T. Tuley, *Radar Cross Section*, 2nd ed. (Scitech Publishing Inc., 2004).
3. T. Liu, Y. Meng, H. Ma, C. Xu, X. Wang, S. Huang, S. Zhao, L. Zheng, and S. Qu, "Simultaneous reduction of microwave reflection and infrared emission enabled by a phase gradient metasurface," Opt. Express **29**, 35891–35899 (2021).
4. N. Lee, J. S. Lim, I. Chang, H. M. Bae, J. Nam, and H. H. Cho, "Flexible assembled metamaterials for infrared and microwave camouflage," Adv. Opt. Mater. **10**, 2200448 (2022).
5. Y.-Z. Wang, H.-X. Xu, C.-H. Wang, M.-Z. Wang, and S.-J. Wang, "Research progress of electromagnetic metamaterial absorbers," Acta Phys. Sinica **69**, 134101 (2020).
6. Q. Yuan, J. M. Jiang, Y. F. Li, C. L. Xu, Y. Cheng, L. X. Jiang, Z. B. Zhu, Z. Qin, H. Wang, J. F. Wang, H. Ma, and S. B. Qu, "The compatible method of designing the transparent ultra-broadband radar absorber with low infrared emissivity," Infrared Phys. Technol. **123**, 104114 (2022).
7. H. Y. Li, H. Yuan, F. Costa, Q. S. Cao, W. Wu, and A. Monorchio, "Optically transparent water-based wideband switchable radar absorber/reflector with low infrared radiation characteristics," Opt. Express **29**, 42863–42875 (2021).
8. H. L. Lv, G. B. Ji, X. G. Li, X. F. Chang, M. Wang, H. G. Zhang, and Y. W. Du, "Microwave absorbing properties and enhanced infrared reflectance of FeAl mixture synthesized by two-step ball-milling method," J. Magn. Magn. Mater. **374**, 225–229 (2015).
9. C. A. Stergiou and G. Litsardakis, "Y-type hexagonal ferrites for microwave absorber and antenna applications," J. Magn. Magn. Mater. **405**, 54–61 (2016).
10. F. Ren, G. M. Zhu, P. G. Ren, K. Wang, X. P. Cui, and X. G. Yan, "Cyanate ester resin filled with graphene nanosheets and $CoFe_2O_4$ reduced graphene oxide nanohybrids as a microwave absorber," Appl. Surf. Sci. **351**, 40–47 (2015).
11. Z. Y. Zhang, M. Z. Xu, X. F. Ruan, J. F. Yan, J. N. Yun, W. Zhao, and Y. N. Wang, "Enhanced radar and infrared compatible stealth properties in hierarchical SnO_2@ZnO nanostructures," Ceram. Int. **43**, 3443–3447 (2017).
12. P. Yu, L. V. Besteiro, Y. Huang, J. Wu, L. Fu, H. H. Tan, C. Jagadish, G. P. Wiederrecht, A. O. Govorov, and Z. Wang, "Broadband metamaterial absorbers," Adv. Opt. Mater. **7**, 1800995 (2018).
13. R. H. Fan, B. Xiong, R. W. Peng, and M. Wang, "Constructing metastructures with broadband electromagnetic functionality," Adv. Mater. **32**, 1904646 (2020).
14. P. P. Min, Z. C. Song, L. Yang, B. Dai, and J. Q. Zhu, "Transparent ultrawideband absorber based on simple patterned resistive metasurface with three resonant modes," Opt. Express **28**, 19518–19530 (2020).
15. C. M. Watts, X. Liu, and W. J. Padilla, "Metamaterial electromagnetic wave absorbers," Adv. Mater. **24**, OP98–OP120 (2012).
16. B. X. Wang, C. Xu, G. Duan, W. Xu, and F. Pi, "Review of broadband metamaterial absorbers: from principles, design strategies, and tunable properties to functional applications," Adv. Funct. Mater. **33**, 2213818 (2023).
17. S. C. Song, X. L. Ma, M. B. Pu, X. Li, Y. H. Guo, P. Gao, and X. G. Luo, "Tailoring active color rendering and multiband photodetection in a vanadium-dioxide-based metamaterial absorber," Photonics Res. **6**, 492–497 (2018).
18. Z. C. Song, P. Min, L. Yang, J. Zhu, and F. Lin, "Wideband diffusion metabsorber for perfect scattering field reduction," Photonics Res. **10**, 1361–1366 (2022).
19. Y. Han, W. Che, X. Xiu, W. Yang, and C. Christopoulos, "Switchable low-profile broadband frequency-selective rasorber/absorber based on slot arrays," IEEE Trans. Antennas Propag. **65**, 6998–7008 (2017).
20. Y. Li, J. Lin, H. Guo, W. Sun, S. Xiao, and L. Zhou, "A tunable metasurface with switchable functionalities: from perfect transparency to perfect absorption," Adv. Opt. Mater. **8**, 1901548 (2020).
21. Z. Luo, X. Ren, L. Zhou, Y. Chen, Q. Cheng, H. F. Ma, and T. J. Cui, "A high-performance nonlinear metasurface for spatial-wave absorption," Adv. Funct. Mater. **32**, 2109544 (2022).
22. Z. Luo, X. Shan, X. Ren, K. Wu, Y. Chen, L. Hong, H. F. Ma, Q. Cheng, and T. J. Cui, "Active metasurface absorber for intensity-dependent surface-wave shielding," IEEE Trans. Antennas Propag. **71**, 5795–5804 (2023).
23. J. Jung, H. Park, J. Park, T. Chang, and J. Shin, "Broadband metamaterials and metasurfaces: a review from the perspectives of materials and devices," Nanophotonics **9**, 3165–3196 (2020).
24. S. B. Glybovski, S. A. Tretyakov, P. A. Belov, Y. S. Kivshar, and C. R. Simovski, "Metasurfaces: from microwaves to visible," Phys. Rep. **634**, 1–72 (2016).
25. Y. I. Abdulkarim, A. Mohanty, O. P. Acharya, B. Appasani, M. S. Khan, S. K. Mohapatra, F. F. Muhammadsharif, and J. Dong, "A review on metamaterial absorbers: microwave to optical," Front. Phys. **10**, 893791 (2022).
26. S. M. Zhong, L. J. Wu, T. J. Liu, J. F. Huang, W. Jiang, and Y. G. Ma, "Transparent transmission-selective radar-infrared bi-stealth structure," Opt. Express **26**, 16466–16476 (2018).
27. C. Zhang, X. Wu, C. Huang, J. Peng, C. Ji, J. Yang, Y. Huang, Y. Guo, and X. Luo, "Flexible and transparent microwave–infrared bistealth structure," Adv. Mater. Technol. **4**, 1900063 (2019).
28. Y. Ma, L. H. Shi, J. B. Wang, L. Y. Zhu, Y. Z. Ran, Y. C. Liu, and J. Li, "A transparent and flexible metasurface with both low infrared emission and broadband microwave absorption," J. Mater. Sci. –Mater. Electron. **32**, 2001–2010 (2021).
29. S. N. Huang, Q. Fan, C. L. Xu, B. K. Wang, J. F. Wang, B. Y. Yang, C. H. Tian, and Z. Meng, "Multiple working mechanism metasurface with high optical transparency, low infrared emissivity and microwave reflective reduction," Infrared Phys. Technol. **111**, 103524 (2020).
30. Z. Q. Gao, C. L. Xu, X. X. Tian, J. F. Wang, H. H. Zhang, S. B. Qu, and Q. Fan, "Multifunctional ultra-thin metasurface with low infrared emissivity, microwave absorption and high optical transmission," Opt. Commun. **500**, 127327 (2021).
31. T. Xiao, C. H. Tian, C. L. Xu, and Z. Q. Gao, "Integrated design of optically transparent composite for low infrared emission and wideband microwave absorption metasurface," Acta Photon. Sinica **51**, 0151117 (2022).
32. C. L. Xu, B. K. Wang, M. B. Yan, Y. Q. Pang, Y. Y. Meng, W. J. Wang, J. F. Wang, Q. Fan, and S. B. Qu, "An optically transparent sandwich structure for radar-infrared bi-stealth," Infrared Phys. Technol. **105**, 103108 (2020).
33. P. Min, Z. Song, L. Yang, V. G. Ralchenko, and J. Zhu, "Multispectral meta-film design: simultaneous realization of wideband microwave absorption, low infrared emissivity, and visible transparency," Opt. Express **30**, 32317–32332 (2022).
34. A. K. Zadeh and A. Karlsson, "Capacitive circuit method for fast and efficient design of wideband radar absorbers," IEEE Trans. Antennas Propag. **57**, 2307–2314 (2009).

35. Y. Zheng, K. Chen, T. Jiang, J. Zhao, and Y. Feng, "Multi-octave microwave absorption via conformal metamaterial absorber with optical transparency," J. Phys. D **52**, 335101 (2019).
36. H. T. Chen, "Interference theory of metamaterial perfect absorbers," Opt. Express **20**, 7165–7172 (2012).
37. C. Zhang, J. Yang, W. Yuan, J. Zhao, J. Y. Dai, T. C. Guo, J. Liang, G. Y. Xu, Q. Cheng, and T. J. Cui, "An ultralight and thin metasurface for radar-infrared bi-stealth applications," J. Phys. D **50**, 444002 (2017).
38. J. B. Sun, L. Y. Liu, G. Y. Dong, and J. Zhou, "An extremely broad band metamaterial absorber based on destructive interference," Opt. Express **19**, 21155–21162 (2011).
39. K. Gao, X. Cao, J. Gao, T. Li, H. Yang, and S. Li, "Ultrawideband metamaterial absorber for oblique incidence using characteristic mode analysis," Photonics Res. **10**, 2751–2759 (2022).
40. Z. Song, J. Zhu, L. Yang, P. Min, and F. H. Lin, "Wideband metasurface absorber (metabsorber) using characteristic mode analysis," Opt. Express **29**, 35387–35399 (2021).
41. Q. Guo, J. Su, Z. Li, J. Song, and Y. Guan, "Miniaturized-element frequency-selective rasorber design using characteristic modes analysis," IEEE Trans. Antennas Propag. **68**, 6683–6694 (2020).
42. R. Zhu, J. Wang, J. Jiang, C. Xu, C. Liu, Y. Jia, S. Sui, Z. Zhang, T. Liu, Z. Chu, J. Wang, T. J. Cui, and S. Qu, "Machine-learning-empowered multispectral metafilm with reduced radar cross section, low infrared emissivity, and visible transparency," Photonics Res. **10**, 1146–1156 (2022).
43. P. P. Min, Z. C. Song, L. Yang, V. G. Ralchenko, and J. Q. Zhu, "Optically transparent flexible broadband metamaterial absorber based on topology optimization design," Micromachines **12**, 1419 (2021).
44. R. Zhu, Z. Zhang, J. Wang, C. Xu, S. Sui, X. Wang, T. Liu, Y. Zhu, L. Zhang, J. Wang, and S. Qu, "Genetic-algorithm-empowered metasurface design: simultaneous realization of high microwave frequency-selection and low infrared surface-emissivity," Opt. Express **29**, 20150–20159 (2021).
45. D. Hu, J. Cao, W. Li, C. Zhang, T. Wu, Q. Li, Z. Chen, Y. Wang, and J. Guan, "Optically transparent broadband microwave absorption metamaterial by standing-up closed-ring resonators," Adv. Opt. Mater. **5**, 1700109 (2017).
46. C. Zhang, Q. Cheng, J. Yang, J. Zhao, and T. J. Cui, "Broadband metamaterial for optical transparency and microwave absorption," Appl. Phys. Lett. **110**, 143511 (2017).
47. C. Zhang, J. Yang, W. Cao, W. Yuan, J. Ke, L. Yang, Q. Cheng, and T. Cui, "Transparently curved metamaterial with broadband millimeter wave absorption," Photonics Res. **7**, 478–485 (2019).
48. Z. C. Song, P. Min, L. Yang, J. Zhu, and F. Lin, "A bilateral coding metabsorber using characteristic mode analysis," IEEE Antennas Wireless Propag. Lett. **21**, 1228–1232 (2022).
49. P. R. West, S. Ishii, G. V. Naik, N. K. Emani, V. M. Shalaev, and A. Boltasseva, "Searching for better plasmonic materials," Laser Photonics Rev. **4**, 795–808 (2010).
50. S. M. Zhong, W. Jiang, P. P. Xu, T. J. Liu, J. F. Huang, and Y. G. Ma, "A radar-infrared bi-stealth structure based on metasurfaces," Appl. Phys. Lett. **110**, 063502 (2017).
51. Z. Meng, C. Tian, C. Xu, J. Wang, X. Li, S. Huang, Q. Fan, and S. Qu, "Optically transparent coding metasurface with simultaneously low infrared emissivity and microwave scattering reduction," Opt. Express **28**, 27774–27784 (2020).
52. T. Liu, Y. Meng, H. Ma, R. Zhu, S. Huang, C. Xu, L. Zhang, J. Wang, and S. Qu, "Broadband surface wave coupler with low infrared emission and microwave reflection," Opt. Express **29**, 35490–35500 (2021).
53. S. D. Gedney, "An anisotropic perfectly matched layer-absorbing medium for the truncation of FDTD lattices," IEEE Trans. Antennas Propag. **44**, 1630–1639 (1996).
54. D. M. Kingsland, J. Gong, J. L. Volakis, and J. F. Lee, "Performance of an anisotropic artificial absorber for truncating finite-element meshes," IEEE Trans. Antennas Propag. **44**, 975–982 (1996).
55. D. Ye, Z. Wang, Z. Wang, K. Xu, B. Zhang, J. Huangfu, C. Li, and L. Ran, "Towards experimental perfectly-matched layers with ultra-thin metamaterial surfaces," IEEE Trans. Antennas Propag. **60**, 5164–5172 (2012).
56. L. D. Landau, E. M. Lifshits, and L. P. Pitaevskii, *Electrodynamics of Continuous Media*, 2nd ed. (Pergamon, 1984).
57. J. B. Pendry, A. J. Holden, D. J. Robbins, and W. J. Stewart, "Magnetism from conductors and enhanced nonlinear phenomena," IEEE Trans. Microw. Theory Tech. **47**, 2075–2084 (1999).
58. J. B. Pendry, A. J. Holden, W. J. Stewart, and I. Youngs, "Extremely low frequency plasmons in metallic mesostructures," Phys. Rev. Lett. **76**, 4773–4776 (1996).
59. D. M. Pozar, *Microwave Engineering*, 2nd ed. (Wiley, 1998).
60. X. X. Tan, J. Chen, and J. X. Li, "A thin and optically transparent infrared-radar compatible stealth structure with low emissivity and broadband absorption," J. Phys. D **55**, 075104 (2022).
61. C. L. Xu, Y. Y. Meng, J. F. Wang, M. B. Yan, W. J. Wang, J. M. Jiang, and S. B. Qu, "Optically transparent hybrid metasurfaces for low infrared emission and wideband microwave absorption," Acta Photon. Sinica **50**, 0416001 (2021).
62. Z. Gao, C. Xu, X. Tian, J. Wang, C. Tian, B. Yang, S. Qu, and Q. Fan, "Ultra-wideband flexible transparent metamaterial with wide-angle microwave absorption and low infrared emissivity," Opt. Express **29**, 22108–22116 (2021).
63. X. Chen, S. Nie, W. Guo, F. Fei, W. Su, W. Gu, and Z. Cui, "Printable high-aspect ratio and high-resolution Cu grid flexible transparent conductive film with figure of merit over 80000," Adv. Electron. Mater. **5**, 1800991 (2019).
64. T. Inagaki and Y. Okamoto, "Surface temperature measurement near ambient conditions using infrared radiometers with different detection wavelength bands by applying a grey-body approximation: estimation of radiative properties for non-metal surfaces," NDT&E Int. **29**, 363–369 (1996).